



Elastic Deformations of Spherical Core-Shell Systems Under an Equatorial Load

Jannis Kolker¹ · Lukas Fischer² · Andreas M. Menzel² · Hartmut Löwen¹

Received: 7 January 2022 / Accepted: 4 May 2022
© The Author(s) 2022

Abstract

Macroscopic elastic core-shell systems can be generated as toy models to be deformed and haptically studied by hand. On the mesoscale, colloidal core-shell particles and microgels are fabricated and investigated by different types of microscopy. We analyse, using linear elasticity theory, the response of spherical core-shell systems under the influence of a line density of force that is oriented radially and acts along the equator of the outer surface. Interestingly, deformational coupling of the shell to the core can determine the resulting overall appearance in response to the forces. We address various combinations of radii, stiffness, and Poisson ratio of core and shell and illustrate the resulting deformations. Macroscopically, the situation could be realized by wrapping a cord around the equator of a macroscopic model system and pulling it tight. On the mesoscale, colloidal microgel particles symmetrically confined to the interface between two immiscible fluids are pulled radially outward by surface tension.

Keywords Linear elasticity theory · Core-shell system · Deformation under external load · Continuum theory

Mathematics Subject Classification 74B10 · 74A10 · 74A30

1 Introduction

Solid sphere-like core-shell systems containing an inner part, the core, of elastic properties different from a surrounding outer part, the shell, are encountered in various contexts on different length scales. On large macroscopic scales, many stars, planets and moons can be approximated by a core and a shell of different elasticity [1]. Jelly sweets covered by a solid layer represent a popular example of not only mechanical or haptic but also culinary experience. Conversely, on the mesoscopic colloidal scale and even down to the nanoscale,

✉ J. Kolker

✉ L. Fischer

¹ Institut für Theoretische Physik II, Heinrich-Heine-Universität Düsseldorf, Universitätsstraße 1, 40225 Düsseldorf, Germany

² Institut für Physik, Otto-von-Guericke-Universität Magdeburg, Universitätsplatz 2, 39106 Magdeburg, Germany

there are numerous soft matter systems involving core-shell particles. These can be prepared in various ways [2, 3] as spherical colloidal particles with a polymer coating [4–6], as micelles [7] or as polymer networks with different crosslinking degrees in the inner and outer part [8–10]. Their controlled fabrication is not only pivotal for applications (such as microreactors [11, 12], targeted drug delivery [13, 14] or smart elastic materials [15, 16]). They also serve as model systems to tailor effective repulsive square-shoulder potentials [17–27] and to understand fundamental questions of statistical mechanics such as freezing and glass formation [4, 28–30].

Our focus in this work is laid on the coupled elastic deformation of inner and outer part, that is core and shell, respectively. We address spherical elastic systems when exposed to a radially oriented force line density along the equatorial circumference of the shell. This setup is motivated by the elasticity problem underlying colloidal core-shell microgel particles that are adsorbed to the interface between two immiscible fluids. At their common contact line, the two fluids pull on the shell of the microgel particle approximately in a radially outward direction in a symmetric setup [31–33]. In many of such interfacial situations, the wetting properties of the surface of a material are crucial for adsorption. A core-shell system provides an appropriate opportunity to adjust by a shell these surface wetting properties to the current need. At the same time, the elastic properties of the core under the influence of an interface are explored. Moreover, the particles may be density matched or functionalized, for example integrating magnetic behaviour, by the selected core material [34–36]. On macroscopic toy model systems, the force densities can be applied by hand, while on even larger, global scales atmospheric effects may lead to equatorially located line-like force densities on planets. An example is the thin area of low atmospheric pressure located around the equator of the earth in the inter-tropical convergence zone. In view of these different systems and situations, the imposed equatorial line force density can either be oriented radially inward (compressive) or radially outward (tensile). In the mathematical treatment this difference is represented by an inversion of the sign of the load.

In this paper, we study the underlying elasticity problem. We present a general continuum theory to compute and predict the shape change of an elastic core-shell system when loaded by an equatorial ring of line force density. Importantly not only the shell deforms, but also the inner core, and the two deformations are coupled to each other by the overall architecture. Through this coupling, the core can influence or even determine the type of deformation of the shell, although the load is applied from outside to the shell, not to the core. We analyse the resulting change of shape in detail, as a function of the relative size of core and shell, different mechanical stiffness of core and shell, as well as their compressibility. In particular, we include the possibility of an elastic *auxetic* response [37–42]. The latter is characterized by a negative Poisson ratio, i.e. when stretched along one axis the system expands along the perpendicular axes. Materials exhibiting corresponding elastic properties have been identified, constructed and analysed [43–46]. In particular it is interesting to consider core and shell materials with different Poisson ratios, as their competition can result in qualitatively different modes of deformation. Our study links to previously investigated geometries, particularly spherical one-component systems [47] or hollow capsules [48] as special cases. Moreover, our additional predictions can be verified by experiments on different scales.

2 Theory and Geometry

Within linear elasticity theory, small deformations of elastic materials are described. The position \mathbf{r} of a material element can be mapped to its position \mathbf{r}' in the deformed state

by adding the displacement vector \mathbf{u} . The displacement field $\mathbf{u}(\mathbf{r})$ in the bulk satisfies the homogeneous Navier-Cauchy equations [49]

$$(1 - 2\nu)\nabla^2\mathbf{u}(\mathbf{r}) + \nabla(\nabla \cdot \mathbf{u}(\mathbf{r})) = \mathbf{0} \tag{1}$$

with $-1 < \nu \leq 1/2$ denoting the Poisson ratio of the elastic substance in three-dimensional situations [50]. Materials with $\nu = 1/2$ are incompressible, while those with negative Poisson ratio are referred to as *auxetic* materials [50]. The latter, when stretched along a certain axis, expand along the lateral directions (instead of undergoing lateral contraction). We ignore any force acting on the bulk, for example gravity. Consequently, in the bulk, the right-hand side of Eq. (1) is set equal to zero.

Furthermore, linear elasticity theory for homogeneous isotropic materials dictates the stress-strain relation [50]

$$\frac{E}{1 + \nu} \left(\underline{\boldsymbol{\varepsilon}}(\mathbf{r}) + \frac{\nu}{1 - 2\nu} \text{Tr}(\underline{\boldsymbol{\varepsilon}}(\mathbf{r})) \underline{\mathbf{I}} \right) = \underline{\boldsymbol{\sigma}}(\mathbf{r}). \tag{2}$$

Equation (2) describes the relationship between the strain tensor $\underline{\boldsymbol{\varepsilon}}(\mathbf{r}) = (\nabla\mathbf{u}(\mathbf{r}) + (\nabla\mathbf{u}(\mathbf{r}))^T)/2$ as the symmetrized gradient of the displacement field $\mathbf{u}(\mathbf{r})$ and the symmetric Cauchy stress tensor $\underline{\boldsymbol{\sigma}}$ (we mark second-rank tensors and matrices by an underscore). E is the Young modulus of the elastic material and $\underline{\mathbf{I}}$ is the unit matrix. The Young modulus E and the Poisson ratio ν are sufficient to quantify the properties of a homogeneous isotropic elastic material.

The boundary conditions at the surface of the elastic shell are

$$\underline{\boldsymbol{\sigma}}(\mathbf{r}) \cdot \mathbf{n} = \frac{\lambda}{R_s} \delta\left(\theta - \frac{\pi}{2}\right) \mathbf{n}. \tag{3}$$

Here, \mathbf{n} describes the outward normal unit vector of the surface and $\delta(\theta - \frac{\pi}{2})/R_s$, with δ the Dirac delta function, sets the location of the line at which the loading force line density of amplitude λ is acting on the core-shell system. We use spherical coordinates so that $\theta = \frac{\pi}{2}$ specifies the equator.

Since we are describing a core-shell material, different elastic properties and radii are attributed to the core and to the shell, see Fig. 1. The core (green) is assigned the radius R_c , the Young modulus E_c , and the Poisson ratio ν_c . The shell (red) is defined by the outer radius R_s , the Young modulus E_s , and the Poisson ratio ν_s . According to Eq. (3), $\lambda > 0$ marks the amplitude of a line density of force pointing radially outward along the equator of the outer surface of the shell.

The system is characterized by the following five dimensionless parameters. First, the ratio $\lambda/E_s R_s$ of the loading force line density on the surface to the Young modulus of the shell describes the relative strength of the load magnitude and is proportional to the amplitude of deformation. The second parameter is the ratio of Young moduli E_c/E_s of the core to the shell and in addition, the two dimensionless Poisson ratios ν_c and ν_s of core and shell, respectively, enter the elasticity theory. The fifth parameter is the size ratio R_c/R_s of the core to the shell.

In spherical coordinates, the position vector \mathbf{r} transforms from the unloaded configuration to the loaded configuration as $\mathbf{r}' = \mathbf{r} + u_r \mathbf{e}_r + u_\theta \mathbf{e}_\theta$, with u_r the radial and u_θ the polar component of the displacement field. \mathbf{e}_r and \mathbf{e}_θ denote the radial and polar unit vector, respectively. Due to the special axial symmetry of the problem, the azimuthal component of the displacement field, u_ϕ , is zero. Concerning the homogeneous Navier-Cauchy equations

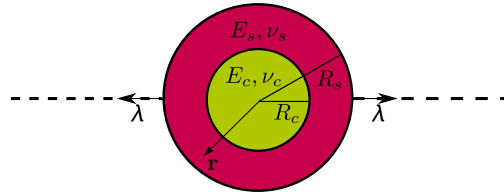


Fig. 1 Schematic visualisation of the core-shell system, here still in its initial spherical shape for illustration. The core (green) is assigned the radius R_c , the Young modulus E_c , and the Poisson ratio ν_c . The shell (red) is described by the outer radius R_s , the Young modulus E_s , and the Poisson ratio ν_s . The system is loaded by exposition to a ring of force line density around the equator of the outer sphere of magnitude λ .

Eq. (1) and the stress-strain relation Eq. (2) recast in spherical coordinates, where in our case the azimuthal dependence vanishes, see the Supporting Information (SI).

For both core and shell we solve Eq. (1) by separation into a series expansion of the polar dependence in terms of Legendre polynomials $P_n(\cos\theta)$ and associated r -dependent prefactors ($r = |\mathbf{r}|$) [51]. We distinguish by superscripts c and s the solutions for core and shell, respectively. More precisely, the solutions [47, 52, 53] of the Navier-Cauchy equations (1) split into a radial component $u_r^{(c)}(\mathbf{r})$ and a polar component $u_\theta^{(c)}(\mathbf{r})$ for the core and take the form

$$u_r^{(c)}(\mathbf{r}) = \sum_{n=0}^{\infty} (a_n^{(c)}(n+1)(-2+n+4\nu_c)r^{n+1} + b_n^{(c)}nr^{n-1}) P_n(\cos\theta), \tag{4}$$

$$u_\theta^{(c)}(\mathbf{r}) = \sum_{n=1}^{\infty} (a_n^{(c)}(5+n-4\nu_c)r^{n+1} + b_n^{(c)}r^{n-1}) \frac{d}{d\theta} P_n(\cos\theta). \tag{5}$$

The solutions for the shell additionally contain terms inverse in the radial distance from the origin

$$u_r^{(s)}(\mathbf{r}) = \sum_{n=0}^{\infty} (a_n^{(s)}(n+1)(-2+n+4\nu_s)r^{n+1} + b_n^{(s)}nr^{n-1} + n(3+n-4\nu_s)c_n^{(s)}r^{-n} - (n+1)d_n^{(s)}r^{-(n+2)}) P_n(\cos\theta), \tag{6}$$

$$u_\theta^{(s)}(\mathbf{r}) = \sum_{n=1}^{\infty} (a_n^{(s)}(5+n-4\nu_s)r^{n+1} + b_n^{(s)}r^{n-1} - (-4+n+4\nu_s)c_n^{(s)}r^{-n} + d_n^{(s)}r^{-(n+2)}) \frac{d}{d\theta} P_n(\cos\theta). \tag{7}$$

As boundary conditions, we use that the traction vectors at the interface of core and shell (at radius R_c) must be equal

$$\underline{\boldsymbol{\sigma}}^{(c)}(R_c\mathbf{e}_r) \cdot \mathbf{n} = \underline{\boldsymbol{\sigma}}^{(s)}(R_c\mathbf{e}_r) \cdot \mathbf{n}. \tag{8}$$

Requiring strict elastic no-slip coupling, also the deformations at the interface must be equal

$$\mathbf{u}^{(c)}(R_c\mathbf{e}_r) = \mathbf{u}^{(s)}(R_c\mathbf{e}_r). \tag{9}$$

Since the Legendre polynomials form a complete orthogonal set, the Dirac delta function in Eq. (3) can be expanded in Legendre polynomials

$$\delta\left(\theta - \frac{\pi}{2}\right) = \sum_{n=0}^{\infty} \frac{2n+1}{2} P_n\left(\cos\left(\frac{\pi}{2}\right)\right) P_n(\cos\theta). \tag{10}$$

Due to the assumed mirror symmetry with respect to the equatorial plane, all odd series expansion components in the core and shell solution in Eqs. (4)-(7) vanish. Therefore we can write for the radial displacement

$$u_r^{(i)}(\mathbf{r}) = u_{r,0}^{(i)}(r) + u_{r,2}^{(i)}(r) P_2(\cos(\theta)) + \dots \tag{11}$$

with $i = c$ for the core and $i = s$ for the shell, respectively. Here, the first component $u_{r,0}^{(i)}(r)$ describes the overall volume change. We note that this term will vanish for $\nu_i \rightarrow 1/2$ and remains as the only component for $\nu_i \rightarrow -1$. The second component gives the first correction to a spherical shape. A positive prefactor $u_{r,2}^{(i)}(r)$ describes a relative prolate deformation while $u_{r,2}^{(i)}(r) < 0$ implies a relative oblate deformation. It is in fact the latter case of an oblate deformation which we expect when the core-shell particle is pulled outwards at the equator ($\lambda > 0$).

The solutions for the displacements of the core and the shell diverge in response to the Dirac delta function at the equator on the surface of the shell, see the boundary condition Eq. (3). Yet, each mode of deformation is only excited to a finite degree by the Dirac delta function, see Eq. (10). Therefore, the second components $u_{r,2}^{(c)}(r)$ and $u_{r,2}^{(s)}(r)$ for the core and the shell remain finite and $u_{r,2}^{(s)}(r)$ is even finite at the surface of the shell. We shall use them as parameters to characterise the relative oblate or prolate deformation of the core and the shell shape.

For convenience, we evaluate these second components at the core and shell radii and normalize them with the corresponding unloaded radii of the core and the shell, respectively. Hence, we use subsequently $u_{r,2}^{(c)}/R_c \equiv u_{r,2}^{(c)}(R_c)/R_c$ and $u_{r,2}^{(s)}/R_s \equiv u_{r,2}^{(s)}(R_s)/R_s$ as dimensionless measures for the shape of the core and the shell.

3 Results and Discussion

3.1 General Solution and Limiting Behaviour

We first present the solutions for the displacements under the prescribed boundary conditions by providing the core coefficients of the expansions (4) and (5)

$$a_n^{(c)} = \frac{\lambda}{E_s R_s} \frac{2n+1}{2} P_n(0) \left(\frac{R_c}{R_s}\right)^{-2} R_s^{-n} \left[\left(\frac{E_c}{E_s}\right) \tilde{c}_{01,n} + \tilde{c}_{02,n} \right] \frac{1}{D}, \tag{12}$$

$$b_n^{(c)} = -\frac{\lambda}{E_s R_s} \frac{2n+1}{2} P_n(0) R_s^{-(n-2)} \left[\left(\frac{E_c}{E_s}\right) \tilde{c}_{03,n} + \tilde{c}_{04,n} \right] \frac{1}{D}, \tag{13}$$

and the shell coefficients of the expansions (6) and (7)

$$a_n^{(s)} = \frac{\lambda}{E_s R_s} \frac{2n+1}{2} P_n(0) R_s^{-n}$$

$$\times \left[\left(\frac{E_c}{E_s} \right)^2 \tilde{c}_{05,n} + \left(\frac{E_c}{E_s} \right) \tilde{c}_{06,n} + \tilde{c}_{07,n} \right] \frac{1}{D}, \tag{14}$$

$$b_n^{(s)} = - \frac{\lambda}{E_s R_s} \frac{2n+1}{2} P_n(0) R_s^{-(n-2)} \times \left[\left(\frac{E_c}{E_s} \right)^2 \tilde{c}_{08,n} + \left(\frac{E_c}{E_s} \right) \tilde{c}_{09,n} + \tilde{c}_{10,n} \right] \frac{1}{D}, \tag{15}$$

$$c_n^{(s)} = \frac{\lambda}{E_s R_s} \frac{2n+1}{2} P_n(0) \left(\frac{R_c}{R_s} \right)^{n-1} R_c^n R_s \times \left[\left(\frac{E_c}{E_s} \right)^2 \tilde{c}_{11,n} + \left(\frac{E_c}{E_s} \right) \tilde{c}_{12,n} + \tilde{c}_{13,n} \right] \frac{1}{D}, \tag{16}$$

$$d_n^{(s)} = - \frac{\lambda}{E_s R_s} \frac{2n+1}{2} P_n(0) \left(\frac{R_c}{R_s} \right)^{n-1} R_c^{n+2} R_s \times \left[\left(\frac{E_c}{E_s} \right)^2 \tilde{c}_{14,n} + \left(\frac{E_c}{E_s} \right) \tilde{c}_{15,n} + \tilde{c}_{16,n} \right] \frac{1}{D}, \tag{17}$$

with

$$D = \left(\frac{E_c}{E_s} \right)^2 \tilde{c}_{17,n} + \frac{E_c}{E_s} \tilde{c}_{18,n} + \tilde{c}_{19,n}. \tag{18}$$

The constants $\tilde{c}_{01,n}$ to $\tilde{c}_{19,n}$ are listed in the SI. In the absence of a core, i.e. $R_c \rightarrow 0$, or in the absence of the shell, i.e. $R_c \rightarrow R_s$, we recover the previous solution for a one-component system as given in Ref. [47]. Also for the special case of $E_c = E_s$ and $\nu_c = \nu_s$ of identical core and shell elasticities, our solution reduces to that of a one-component system.

3.2 Relative Deformation of the Shell and the Core

In the following, the degrees of deformation of the core and the shell are investigated for volume conserving conditions ($\nu_c = \nu_s = 1/2$) for both tensile ($\lambda > 0$) and compressive ($\lambda < 0$) situations. Figure 2 shows the relative deformation $u_{r,2}^{(i)}/R_i$ for a tensile (left column) and a compressive (right column) line force density. The relative deformation is plotted for the shell ($i = s$) in a) and b) and for the core ($i = c$) in c) and d) as a function of the ratios of Young moduli E_c/E_s . Data are provided for several size ratios R_c/R_s ranging from 0.3 to 1.

The first observation is that the coefficient $u_{r,2}^{(i)}/R_i$ is negative for the tensile case and positive for a compressive situation, corresponding to a relative oblate and prolate deformation. This is a simple consequence of the force load pulling or pushing the equator to the outward or inward direction, respectively.

Second, the absolute magnitude of deformation decreases in both cases with increasing E_c/E_s which is the expected trend if the core is getting harder than the shell (at fixed shell elasticity). For $E_c/E_s \rightarrow 0$ we obtain the special case of a hollow sphere. In this limit, the relative deformation of the core and the shell reaches a finite saturation (note the logarithmic scale in Fig. 2). In the opposite limit $E_c/E_s \rightarrow \infty$ the core gets rigid, which implies that the displacement of the shell stays finite but the displacement of the core tends to zero. We find a common finite slope of ± 1 for the curves associated with the core for $E_c/E_s \rightarrow \infty$ in Fig. 2.

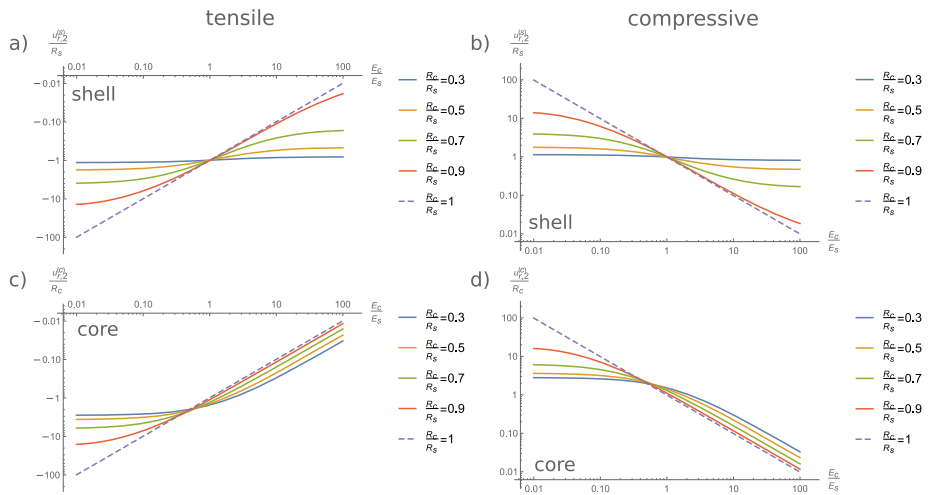


Fig. 2 Relative deformation $u_{r,2}^{(i)}/R_i$ as a function of the ratio of Young moduli E_c/E_s at different size ratios R_c/R_s . Two cases are considered, namely **a,c**) tensile (oriented radially outward, $\lambda/(E_s R_s) = 1$) and **b,d**) compressive (oriented radially inward, $\lambda/(E_s R_s) = -1$) line force densities. For both cases the relative deformation of the shell ($i = s$) in **a**) and **b**) and the core ($i = c$) in **c**) and **d**) is shown on a double logarithmic scale. Further parameters are $\nu_c = \nu_s = 1/2$. The blue dashed line corresponds to the limit of a one-component system (for $R_c/R_s = 1$).

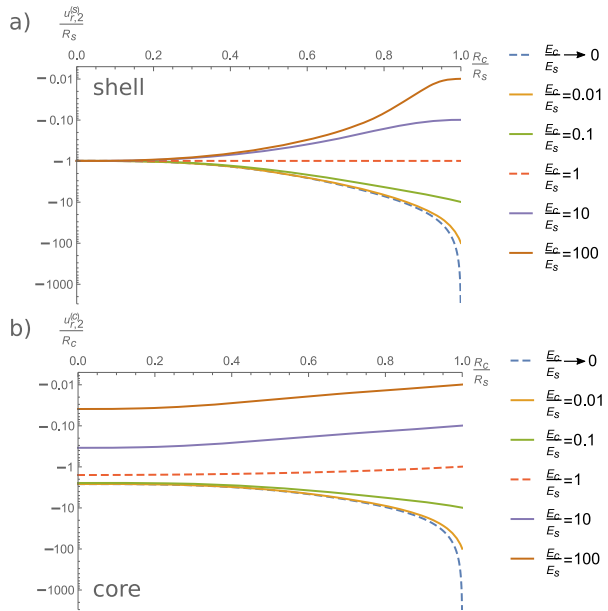
Moreover, in Fig. 2a all curves intersect in the same point at $E_c = E_s$. At this point the two materials are identical and the size ratio becomes irrelevant for the deformation at the shell surface. The curves of Fig. 2b do not exhibit a common intersection point due to our normalization of the relative deformation with R_c and the fact that the radial deformation is in general not homogeneous along the radius. For increasing R_c/R_s , the influence of the core grows and the curves exhibit more sensitivity as a function of E_c for fixed E_s .

To complement the picture, Fig. 3 shows the same quantity as in Fig. 2 for the tensile case, namely the relative oblate deformation $u_{r,2}^{(i)}/R_i$, but now as a function of the size ratio R_c/R_s for a) the shell ($i = s$) and b) the core ($i = c$). Curves for several ratios of Young moduli E_c/E_s are displayed. For $E_c = E_s$ (dashed red curves), the resulting effective one-component system features a shell displacement that does not depend on the size ratio of core to shell. Conversely, the plotted core displacement does depend on the size ratio for $E_c = E_s$ because it is normalized by the size of the core. The deformation scaled by R_c in the limit of small core size $R_c \rightarrow 0$ (see Fig. 3b) reaches different limits for different ratios of Young moduli although the core becomes vanishingly small. Furthermore, the limit of a hollow sphere system $E_c/E_s \rightarrow 0$, is also shown in Fig. 3a) and b).

3.3 Deformational Behaviour for Different Poisson Ratios of Core and Shell

We now study the different deformation behaviour for the core and the shell with respect to their Poisson ratios. In particular we explore the elastic response for an auxetic core combined with a regular elastic shell, and vice versa. Such combinations can, at least, be realized in macroscopic elastic model systems, when appropriate materials are chosen. Thus their behaviour is investigated systematically for varying compressibility and auxetic properties. Figure 4 shows the deformational behaviour of the core and the shell as a function of their (in general different) Poisson ratios ν_c and ν_s . For simplicity we here consider the same

Fig. 3 Relative oblate deformation $u_{r,2}^{(i)}/R_i$ as a function of the size ratio R_c/R_s for different ratios of Young moduli E_c/E_s for a) the shell ($i = s$) and b) the core ($i = c$) on semi-logarithmic scale. Further parameters are $\nu_c = \nu_s = 1/2$ and $\lambda/(E_s R_s) = 1$. The red ($E_c/E_s = 1$) and blue ($E_c/E_s \rightarrow 0$) dashed curves correspond to one-component and hollow sphere systems, respectively.



stiffness of the core and the shell, $E_c = E_s$. Moreover we fix the core size to $R_c = 0.5R_s$ and the load amplitude to $\lambda/(E_s R_s) = 0.1$.

We distinguish between two different states of the displacement: I) the shell is more oblate than the core and II) the core is more oblate than the shell. In order to do so, we use the absolute value of the (here always negative) second coefficient of relative deformation of the shell $|u_{r,2}^{(s)}/R_s|$ and the core $|u_{r,2}^{(c)}/R_c|$. For state I) (reddish and greenish in Fig. 4) we have $|u_{r,2}^{(s)}/R_s| > |u_{r,2}^{(c)}/R_c|$, while for state II) (greyish in Fig. 4) we have $|u_{r,2}^{(s)}/R_s| < |u_{r,2}^{(c)}/R_c|$. See also the two schematic sketches on the top right-hand side of Fig. 4. The transition from I) to II), given by the same relative degree of oblate deformation $|u_{r,2}^{(s)}/R_s| = |u_{r,2}^{(c)}/R_c|$, is shown in Fig. 4 by the yellow line separating the two regions. There is a non-monotonic behaviour of this line as a function of ν_c for an auxetic shell ($\nu_s \approx -0.6$) and a nearly incompressible core.

The different colour codes on the right hand side in Fig. 4 represent the magnitude of the relative oblate deformation of the shell for state I) and of the core for state II). For nine selected points indicated in the $\nu_c \nu_s$ -plane we illustrate the corresponding shapes of the core and the shell as given by the components $u_{r,0}^{(c)}, u_{r,2}^{(c)}, u_{r,0}^{(s)}$ and $u_{r,2}^{(s)}$, respectively, describing the change in volume and relative oblate deformation.

At the origin in the state diagram, where $\nu_c = \nu_s = 0$, the relative oblate deformation of the core and the shell are equal so that the yellow line passes through the origin in Fig. 4. Strictly speaking, this point [and all others on the diagonal from (a) to (d)] describes a one-component system, because there the elastic properties of the core and the shell are identical. We note that in general the yellow line of $|u_{r,2}^{(s)}/R_s| = |u_{r,2}^{(c)}/R_c|$ does not coincide with the diagonal of $\nu_c = \nu_s$ in Fig. 4, although we find a one-component material in the latter case. One aspect that contributes to this result is the inhomogeneous stress and strain distribution in the system, resulting from the force density that is concentrated at the equator. Further remarks on these stress and strain distributions are given in Sect. 3.4.

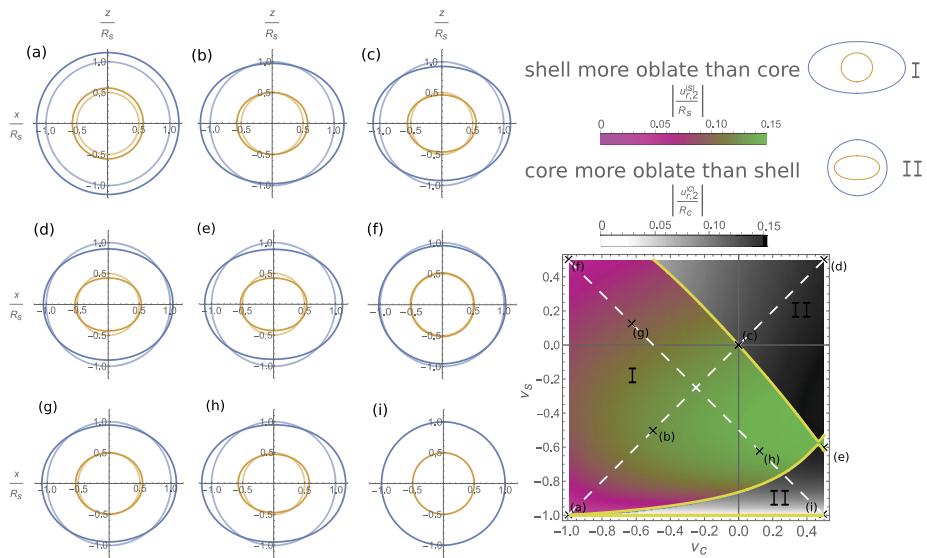


Fig. 4 Bottom right: State diagram exhibiting two situations I) and II) in the plane spanned by the two Poisson ratios of the core ν_c and the shell ν_s at fixed $E_c = E_s$, $R_c = 0.5R_s$ and $\lambda/(E_s R_s) = 0.1$. In I), corresponding to the reddish and greenish region, the relative oblate deformation of the shell is larger in magnitude than that of the core, see schematic representation on the top right. Here we plot in region I) of the state diagram $|u_{r,2}^{(s)}/R_s|$ as colour-coded on the top right. Conversely, in II), corresponding to the greyish region in the state diagram, the relative oblate deformation of the core is larger in magnitude than that of the shell. Here we plot in region II) of the state diagram $|u_{r,2}^{(c)}/R_c|$ as colour-coded on the top right. The two states I) and II) are separated by yellow lines, which represent the same relative degree of oblate deformation. Effectively, a one-component system is given by the (white dashed) diagonal from (a) to (d). Furthermore, for nine parameter combinations indicated for various points (a)-(i) in the state diagram, the corresponding elliptical shapes of core and shell are shown on the left with the light curves as a reference to the undeformed system.

Clearly, for the parameter combinations on the yellow line separating regions I) and II), the relative oblate deformations of core and shell are equal, as seen in Fig. 4 (a), (c), and (i) ($|u_{r,2}^{(s)}/R_s| = |u_{r,2}^{(c)}/R_c|$). In the special cases of (a) and (i) we recover spherical shapes of core and shell, even if the volume has changed ($|u_{r,2}^{(c)}/R_c| = |u_{r,2}^{(s)}/R_s| = 0$). We observe that $|u_{r,2}^{(c)}/R_c|$ and $|u_{r,2}^{(s)}/R_s|$ in the state diagram are continuous when varying the Poisson ratios, even in the vicinity of (e). For $\nu_s = -1$, we found that the shell determines the considered modes $u_{r,2}^{(c)}$ and $u_{r,2}^{(s)}$, forcing them to vanish. In conclusion, different Poisson ratios can largely tune the behaviour of the core-shell structure under external loading.

3.4 Internal Stress Field

We now provide explicit data for the internal stress field. For quasi volume conserving conditions ($\nu_c = \nu_s = 0.4999$), a size ratio of $R_c/R_s = 0.5$, and an amplitude of $\lambda/(E_s R_s) = 0.1$ of the force line density, loaded configurations of the core-shell system for three different ratios of Young moduli E_c/E_s are shown in Fig. 5.

The loaded configurations are colour coded for the components of the (symmetric) stress tensor, defined by $\underline{\sigma}^{(i)} = \sigma_{rr}^{(i)} \mathbf{e}_r \otimes \mathbf{e}_r + \sigma_{r\theta}^{(i)} (\mathbf{e}_\theta \otimes \mathbf{e}_r + \mathbf{e}_r \otimes \mathbf{e}_\theta) + \sigma_{\theta\theta}^{(i)} \mathbf{e}_\theta \otimes \mathbf{e}_\theta$, for the core

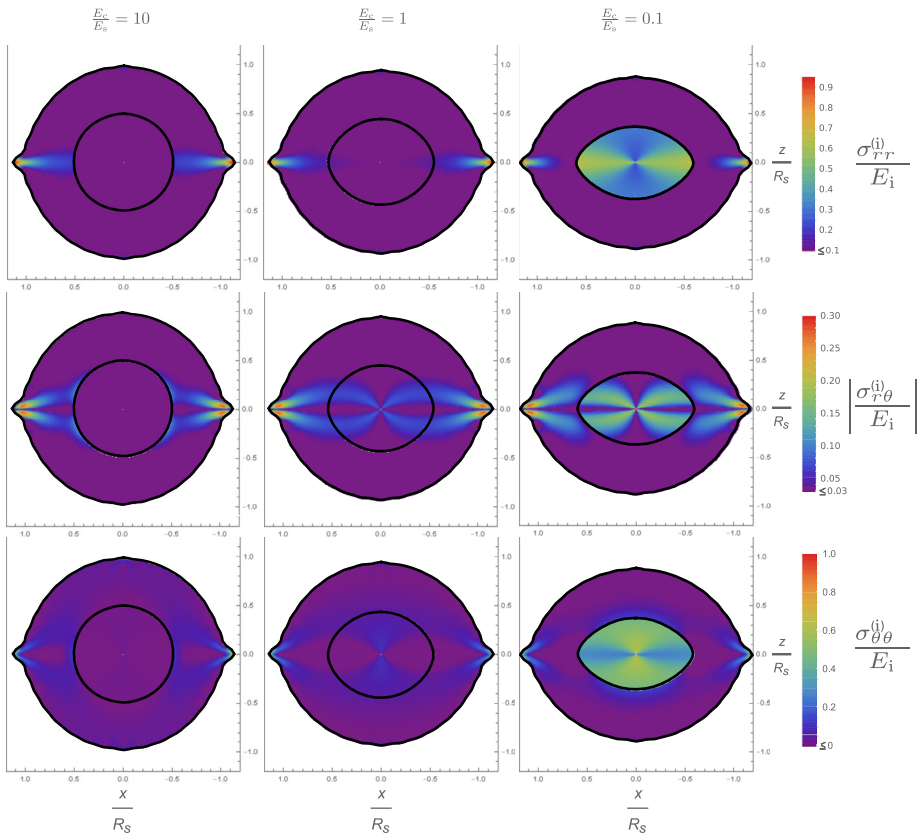


Fig. 5 Loaded configurations of the core-shell system at fixed $\nu_c = \nu_s = 0.4999$, $R_c = 0.5R_s$, and $\lambda/(E_s R_s) = 0.1$. The colour code reflects the three scaled components of the symmetric stress tensor $\sigma_{rr}^{(i)}/E_i$, $|\sigma_{r\theta}^{(i)}|/E_i$ and $\sigma_{\theta\theta}^{(i)}/E_i$ for the core ($i = c$) and the shell ($i = s$). Three different ratios of Young moduli E_c/E_s each are shown for the three components. The core and shell boundaries are indicated by black lines. To achieve a better resolution, only the absolute value of $\sigma_{r\theta}^{(i)}/E_i$ is shown. By symmetry, this tensor component changes sign in the different quadrants of the xz -plane.

($i = c$) and the shell ($i = s$). The components of the stress tensor are scaled by the respective E_i in the core ($i = c$) and in the shell ($i = s$). Results for the deformations and associated components of stress are calculated from Eqs. (2) and (4)–(7), where the infinite series are truncated at $n = 32$.

For all configurations, all components of the stress tensor are of the greatest extent around the equatorial line of loading along the shell surface. Clearly, the system there experiences a displacement in positive radial (outward) direction. Due to the quasi-incompressibility of both shell and core, a strong degree of inverted displacement results at the poles.

For $E_c \ll E_s$, the soft core deforms more easily than the surrounding harder shell and experiences a higher amount of scaled stress. The scaled stress of the quasi-incompressible shell is transferred from the equator towards the inside by the bulk elasticity of the shell (see the right column in Fig. 5). Conversely, for $E_c \gg E_s$, there is hardly any influence of the deformation of the shell on the core for the scaled stresses (see the left column in Fig. 5).

For comparison, the center column in Fig. 5 shows a loaded one-component system $E_c = E_s$ and the corresponding scaled components of stress.

4 Conclusions

We have analysed in detail the deformational response of an elastic core-shell system to a radially oriented force line density acting along the outside equatorial line. Natural extensions of our considerations include the following.

First, the axially symmetric situation that we addressed could be generalized to systems exposed to line densities that are modulated along the circumference. Moreover, the effect of surface force densities applied in patches or distributed over the whole surface area could be analysed, instead of pure force line densities. In a further step, the imposed distortions may not only be imposed from outside, but could additionally result from internal active or actuation centers. Obvious candidates for corresponding actuatable cores are given by magnetic gels [54, 55]. For these types of systems, magnetically induced deformations have already been analysed by linear elasticity theory in the case of one-component elastic spheres [56–58].

The considered geometry of loading can effectively be realised in experiments on the mesoscale by exposing core-shell microgel particles to the interface between two immiscible fluids acting on the elastic system [32, 33]. There, interfacial tension radially pulls on the equatorial circumference along the common contact line in a symmetric setup. Yet, our description can be applied to any system on any scale that can be characterized by continuum elasticity theory. For example, macroscopic elastic core-shell spheres could be generated as toy models using soft transparent elastic shells on an elastic core. The line of loading force could then simply be imposed by tying a cord around the equator of these macroscopic core-shell spheres and tightening it. In this setup, the direction of the force is inverted as well. However, this in our evaluation simply means that all directions of displacement are inverted. Such macroscopic approaches may support the involvement of auxetic components [37–42]. Depending on the materials at hand, this strategy may facilitate the experimental confirmation of our results, possibly by direct visual inspection.

Supplementary Information The online version contains supplementary material available at <https://doi.org/10.1007/s10659-022-09897-1>.

Acknowledgements L.F. and A.M.M. thank the Deutsche Forschungsgemeinschaft (DFG) for support through the SPP 1681 on magnetic hybrid materials, grant no. ME 3571/2-3, and for support through the Heisenberg Grant ME 3571/4-1 (A.M.M.). H.L. acknowledges funding from the Deutsche Forschungsgemeinschaft (DFG) under grant number LO 418/22-1.

Funding Note Open Access funding enabled and organized by Projekt DEAL.

Open Access This article is licensed under a Creative Commons Attribution 4.0 International License, which permits use, sharing, adaptation, distribution and reproduction in any medium or format, as long as you give appropriate credit to the original author(s) and the source, provide a link to the Creative Commons licence, and indicate if changes were made. The images or other third party material in this article are included in the article's Creative Commons licence, unless indicated otherwise in a credit line to the material. If material is not included in the article's Creative Commons licence and your intended use is not permitted by statutory regulation or exceeds the permitted use, you will need to obtain permission directly from the copyright holder. To view a copy of this licence, visit <http://creativecommons.org/licenses/by/4.0/>.

References

1. Jacobs, J.: The Earth's Core. *Int. Geophys.* **20**, 213–237 (1975)
2. Caruso, F.: *Adv. Mater.* **13**, 11–22 (2001)
3. Schärfl, W.: *Nanoscale* **2**, 829–843 (2010)
4. Pusey, P.N.: In: Hansen, J.P., Levesque, D., Zinn-Justin, J. (eds.) *Liquids, Freezing and the Glass Transition*. North-Holland, Amsterdam (1991)
5. Lekkerkerker, H.N., Tuinier, R.: In: *Colloids and the Depletion Interaction*, pp. 57–108. Springer, Dordrecht (2011)
6. Royall, C.P., Poon, W.C., Weeks, E.R.: *Soft Matter* **9**, 17–27 (2013)
7. Förster, S., Abetz, V., Müller, A.H.: In: *Polyelectrolytes with Defined Molecular Architecture II. Advances in Polymer Science*, vol. 166, pp. 173–210. Springer, Berlin (2004)
8. Rey, M., Fernandez-Rodriguez, M.A., Karg, M., Isa, L., Vogel, N.: *Acc. Chem. Res.* **53**, 414–424 (2020)
9. Rey, M., Hou, X., Tang, J.S.J., Vogel, N.: *Soft Matter* **13**, 8717–8727 (2017)
10. Plamper, F.A., Richtering, W.: *Acc. Chem. Res.* **50**, 131–140 (2017)
11. Yang, Z., Yang, L., Zhang, Z., Wu, N., Xie, J., Cao, W.: *Colloids Surf. A, Physicochem. Eng. Asp.* **312**, 113–117 (2008)
12. Liu, N., Zhao, S., Yang, Z., Liu, B.: *ACS Appl. Mater. Interfaces* **11**, 47008–47014 (2019)
13. Kataoka, K., Harada, A., Nagasaki, Y.: *Adv. Drug Deliv. Rev.* **47**, 113–131 (2001)
14. Bonacucina, G., Cespi, M., Misici-Falzi, M., Palmieri, G.F.: *J. Pharm. Sci.* **98**, 1–42 (2009)
15. Motornov, M., Roiter, Y., Tokarev, I., Minko, S.: *Prog. Polym. Sci.* **35**, 174–211 (2010)
16. Förster, S., Plantenberg, T.: *Angew. Chem., Int. Ed.* **41**, 688–714 (2002)
17. Heyes, D., Aston, P.: *J. Chem. Phys.* **97**, 5738–5748 (1992)
18. Bolhuis, P., Frenkel, D.: *J. Phys. Condens. Matter* **9**, 381–387 (1997)
19. Denton, A., Löwen, H.: *J. Phys. Condens. Matter* **9**, L1 (1997)
20. Jagla, E.: *Phys. Rev. E* **58**, 1478–1486 (1998)
21. Malescio, G., Pellicane, G.: *Nat. Mater.* **2**, 97–100 (2003)
22. Pauschenwein, G.J., Kahl, G.: *J. Chem. Phys.* **129**, 174107 (2008)
23. Yuste, S.B., Santos, A., López de Haro, M.: *Mol. Phys.* **109**, 987–995 (2011)
24. Norizoe, Y., Kawakatsu, T.: *J. Chem. Phys.* **137**, 024904 (2012)
25. Pattabhiraman, H., Gantapara, A.P., Dijkstra, M.: *J. Chem. Phys.* **143**, 164905 (2015)
26. Gabriëlse, A., Löwen, H., Smalenburg, F.: *Materials* **10**, 1280 (2017)
27. Somerville, W.R., Law, A.D., Rey, M., Vogel, N., Archer, A.J., Buzza, D.M.A.: *Soft Matter* **16**, 3564–3573 (2020)
28. Ivlev, A., Morfill, G., Löwen, H., Royall, C.P.: *Complex Plasmas and Colloidal Dispersions: Particle-resolved Studies of Classical Liquids and Solids*, vol. 5. World Scientific, Singapore (2012)
29. Gasser, U.: *J. Phys. Condens. Matter* **21**, 203101 (2009)
30. Karg, M., Pich, A., Hellweg, T., Hoare, T., Lyon, L.A., Crassous, J., Suzuki, D., Gumerov, R.A., Schneider, S., Potemkin, I.I., Richtering, W.: *Langmuir* **35**, 6231–6255 (2019)
31. Bresme, F., Oettel, M.: *J. Phys. Condens. Matter* **19**, 413101 (2007)
32. Harrer, J., Rey, M., Ciarella, S., Löwen, H., Janssen, L.M.C., Vogel, N.: *Langmuir* **35**, 10512–10521 (2019)
33. Kolker, J., Harrer, J., Ciarella, S., Rey, M., Ickler, M., Janssen, L.M.C., Vogel, N., Löwen, H.: *Soft Matter* **17**, 5581–5589 (2021)
34. Rauh, A., Rey, M., Barbera, L., Zanini, M., Karg, M., Isa, L.: *Soft Matter* **13**, 158–169 (2017)
35. Vasudevan, S.A., Rauh, A., Kroger, M., Karg, M., Isa, L.: *Langmuir* **34**, 15370–15382 (2018)
36. Huang, S., Gawlitza, K., von Klitzing, R., Gilson, L., Nowak, J., Odenbach, S., Steffen, W., Auernhammer, G.K.: *Langmuir* **32**, 712–722 (2016)
37. Huang, C., Chen, L.: *Adv. Mater.* **28**, 8079–8096 (2016)
38. Ren, X., Das, R., Tran, P., Ngo, T.D., Xie, Y.M.: *Smart Mater. Struct.* **27**, 023001 (2018)
39. Scarpa, F., Bullough, W., Lumley, P.: *Proc. Inst. Mech. Eng., Part C, J. Mech. Eng. Sci.* **218**, 241–244 (2004)
40. Lakes, R.: *Science* **235**, 1038–1041 (1987)
41. Chan, N., Evans, K.: *J. Mater. Sci.* **32**, 5945–5953 (1997)
42. Caddock, B., Evans, K.: *J. Phys. D, Appl. Phys.* **22**, 1877–1882 (1989)
43. Babae, S., Shim, J., Weaver, J.C., Chen, E.R., Patel, N., Bertoldi, K.: *Adv. Mater.* **25**, 5044–5049 (2013)
44. Jiang, Y., Li, Y.: *Sci. Rep.* **8**, 2397 (2018)
45. Kim, Y., Yuk, H., Zhao, R., Chester, S.A., Zhao, X.: *Nature* **558**, 274–279 (2018)
46. Evans, K.E.: *Endeavour* **15**, 170–174 (1991)
47. Style, R.W., Isa, L., Dufresne, E.R.: *Soft Matter* **11**, 7412–7419 (2015)
48. Hegemann, J., Boltz, H.-H., Kierfeld, J.: *Soft Matter* **14**, 5665–5685 (2018)

49. Cauchy, A.L.B.: Exercices de mathématiques. De Bure Frères, vol. 3. (1828)
50. Landau, L., Lifshitz, E.: Theory of Elasticity, 3rd edn. Butterworth-Heinemann, Oxford (1986)
51. Love, A.E.H.: A Treatise on the Mathematical Theory of Elasticity. Cambridge University Press, Cambridge (1927)
52. Duan, H.L., Wang, J., Huang, Z.P., Karihaloo, B.L.: Proc. R. Soc. A, Math. Phys. Eng. Sci. **461**, 3335–3353 (2005)
53. Yi, X., Duan, H.L., Karihaloo, B.L., Wang, J.: Arch. Mech. **59**, 259–281 (2007)
54. Weeber, R., Hermes, M., Schmidt, A.M., Holm, C.: J. Phys. Condens. Matter **30**, 063002 (2018)
55. Odenbach, S.: Arch. Appl. Mech. **86**, 269–279 (2016)
56. Fischer, L., Menzel, A.M.: J. Chem. Phys. **151**, 114906 (2019)
57. Fischer, L., Menzel, A.M.: Phys. Rev. Res. **2**, 023383 (2020)
58. Fischer, L., Menzel, A.M.: Smart Mater. Struct. **30**, 014003 (2021)

Publisher's Note Springer Nature remains neutral with regard to jurisdictional claims in published maps and institutional affiliations.